

REFLECTIVE MODE FOURIER PTYCHOGRAPHY

by

Basel Salahieh

Committee Members

Rongguang Liang (Chair), Jeffrey Rodriguez (Member), Tom Milster (Member)

Copyright © Basel Salahieh 2015

A Master's Report Submitted to the College of the

OPTICAL SCIENCES

In Partial Fulfillment of the Requirements

For the Degree of

MASTER OF SCIENCE

In the Graduate College

THE UNIVERSITY OF ARIZONA

2015

Table of Contents

List of Figures	3
Abstract	4
Overview of Reflective Imaging Systems	5
Background in Optics	5
Limitations of Conventional Imaging Systems.....	6
Introduction to Fourier Ptychography.....	7
Algorithm.....	7
Simulating the Iterative FP Algorithm.....	9
Case Studies on Selected FP Parameters	11
Impact of Superresolution Factor.....	11
Impact of the Update Path.....	12
Impact of Circular Path Radius.....	14
Impact of Number of LR Images	15
Experimental Results	17
XY Measurements	18
Circular Measurements	21
Fourier Ptychography for Diffusing Objects	23
Conclusion and Future Research Directions.....	25
Acknowledgement	27
References.....	28

List of Figures

Fig. 1. The imaging path in reflective imaging systems.	5
Fig. 2. Iterative recovery procedure of the Fourier Ptychography algorithm.	8
Fig. 3. A complex HR scene (left), its Fourier transform (center), and samples of LR images (right). The LR images are framed in different colors to indicate their correspondent locations in the Fourier space.	9
Fig. 4. Iterative reconstruction results for intensity (first row), phase (second row), and the frequency space showing the circle profile being updated (third row). The original phase was scaled between $(-\pi, \pi)$	10
Fig. 5. Final FP reconstructions of cameraman intensity and aerial phase images after median filtering with original phase scaled to $(-\pi, \pi)$ (left), to $(-\pi/2, \pi/2)$ (center), and reconstruction errors as function of iteration index (right).	10
Fig. 6. Iterative reconstruction results for USAF (zoomed) at different SR factors.	12
Fig. 7. Iterative reconstruction errors as a function of iteration index for various SR factors. ...	12
Fig. 8. Iterative reconstruction results for USAF (zoomed) at different update paths.	13
Fig. 9. Update paths (left) and the associated iterative reconstruction errors as a function of iteration index (right).	13
Fig. 10. Iterative reconstruction results for USAF (zoomed) at different path radii.	15
Fig. 11. Circular paths of different radii in pixels (left) and the associated iterative reconstruction errors as a function of iteration index (right).	15
Fig. 12. Reconstruction results for USAF (zoomed) after 33% and 100% of iterations at different # measurements (across the rows) for two different update paths; the circular path (first two columns) and outward spiral path (last two columns).	16
Fig. 13. Update paths (left column) and iterative reconstruction errors as a function of normalized iteration index (right column) for different number of images taken in a circular path (top row) and in an outward spiral path (bottom row).	16
Fig. 14. Sketch (left) and the experimental relective-mode imaging setup (right) showing the XY and Circ illuminations.	17
Fig. 15. 9×9 LR Images captured by XY translations of a green LED.	18
Fig. 16. FP using XY measurements; LR centered patch (top-left), and its FP reconstruction (top-right), 3×3 LR patches (bottom-left), and their FP reconstructed image after stitching (bottom-right).	19
Fig. 17. FP reconstructions at selected images and circular paths. The selected locations are shown at the bottom-left of each image. The whole spiral update path is shown at the bottom-right image.	20
Fig. 18. 72 LR images captured by a circular translation of a green LED.	21
Fig. 19. FP using circular measurements; circular path (top-left), FP reconstruction for the centered patch (top-right), LR Image (bottom-left), and its 3×3 patch FP reconstructed image (bottom-right).	22
Fig. 20. A reflection sample of diffusing surface (left) and the correspondent frequency regions in Fourier space (right).	23
Fig. 21. USAF target with Optispray diffusing material on it to emulate diffusion (left), sample of LR image taken with $N_{Ameas}= 0.037$ (center), and the resulted FP reconstruction of $N_{Asynth}= 0.1$ (right).	24

Abstract

Reflective surface metrology is the measurement of small-scale features on surfaces through reflective imaging systems. Such surfaces may be in difficult-to-reach places (e.g. inside machines), hence fiberscopes are required for the inspection. However, the need to capture large extent of the surfaces by a physically restricted image sensor results in low-resolution (LR) measurements which prevent accurate analyses. The light in traditional reflective imaging systems is emitted from a light source at certain angle, reflected from a partially diffusing object, and captured by the image sensor. In this report, we investigate the role of computational illumination in retrieving the fine details of reflective surfaces from a set of LR measurements, each taken at different illumination angle.

Fourier Ptychography (FP) is an aperture-synthesizing imaging technique that iteratively stitches together a number of variably illuminated, LR intensity images in the Fourier space to produce a wide-field, high-resolution (HR) complex image. FP was first introduced in the transmittive-mode microscopy but here it is being investigated for the reflective-mode metrology

As a simulation study, the impact of the targeted superresolution factor, the update path, the circular path radius, and the number of LR measurements on the iterative FP technique were evaluated. In the experimental setup, the illumination angle was actively controlled by either translating the light source in XY directions to collect the central bright field measurements or rotating it in a circular trajectory around the objective lens to collect the dark field information.

The simulation and experimental results show the capability of resolving finer features with more measurements illuminated at steeper angles, the fast convergence when updating the HR Fourier space following an outward spiral path, and the ability to synthesize a numerical aperture (NA) of 0.235 from 81 LR images captured by a 0.1 NA objective lens.

Overview of Reflective Imaging Systems

The imaging path of reflective-mode inspection devices, shown in Fig. 1, features a light source that emits a coherent light (approximated as plane wave at certain direction), partially diffusing object upon which the light is reflected, objective lens to image the object through its numerical aperture (NA) and field of view (FOV), and a focal planar array to capture the image at its subsampling resolution.

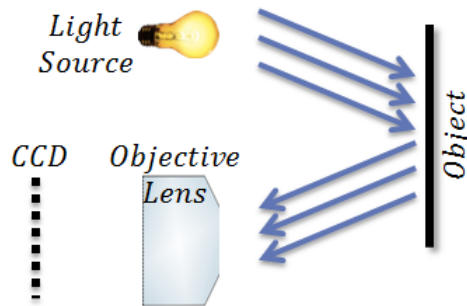


Fig. 1. The imaging path in reflective imaging systems.

Background in Optics

The objective lens through its NA acts as a low pass filter with optical resolution set by the diffraction limit (assuming no aberrations) given in Rayleigh criterion as $R = 0.61 \lambda / NA$ where λ is the wavelength of light. The image sensor, according to Nyquist criterion, has to at least sample at half the smallest feature size R so no aliasing is induced. Thus, a smaller pixel size of the image sensor is desired but this may also impose limitations on the dynamic range and the signal-to-noise ratio collected from each detector. On other hand, the imaging lens also sets the FOV, the depth of field (DOF), and the magnification of the captured scene. These define how many image pixels are used to sample a certain region in the object space.

Limitations of Conventional Imaging Systems

The number of resolvable points (imaging throughput) of the conventional optical systems can be characterized by the space-bandwidth product (SBP) [1] (confounded by the scale-dependent geometric aberrations) which in turn features an inherent design conflict; i.e. a better resolution (larger NA, larger bandwidth) implies smaller FOV and narrower DOF (smaller space) [2] given a fixed focal length and finite detector array. Thus, there is a need for computational imaging techniques to break such traditional limitations.

Inspection imaging devices such as fiberscopes are usually designed to cover a wide angle of view $\sim 120^\circ$ (relatively large FOV) but are also physically restricted in the lens aperture and the sensor size which results in small NA and low-resolution (LR) acquisition. Therefore, accurate image analyses are difficult to be achievable as the fine features are not being captured.

Superresolution (SR) techniques are employed to retrieve the high-resolution (HR) details beyond the diffraction limit mandated by the imaging optics and the sensing medium [3] from a set of multiple LR images. Each LR image has to contribute with additional information which may be attained by varying the illumination conditions with respect to other LR measurements.

In this report, the possibility of recovering higher resolution by varying the direction of illuminating rays for each captured LR image is investigated for a reflective-mode imaging setup.

Introduction to Fourier Ptychography

Fourier Ptychography (FP) [2, 4] is a computational illumination technique that is capable of providing a scalable SBP to overcome the physical limitations of the optical systems by using a plurality of images acquired at different illumination conditions (e.g. incident angles of illuminating rays). FP enables one to use a low NA objective, having a large FOV, but still obtain HR across the entire image. It works by iteratively expanding SBP in the Fourier space via multi-image fusion, similar to synthetic aperture microscopy [5], to recover a richer output complex image. Besides the superresolution with large FOV (which is the main interest in this report), FP can also be considered a phase retrieval algorithm [6], a 3D intensity and phase reconstruction technique [7], a digital refocusing method [8], a wavefront correction routine [4], and a pupil recovery procedure [9].

Algorithm

A set of N variably illuminated raw intensity images is sequentially captured by a low NA_{meas} objective, which provides a longer working distance and larger depth of field at the expense of a lower spatial resolution. Each illumination from a unique angle, approximated as a plane wave with unique phase, corresponds to a shift proportional to the angle of illumination in the Fourier space. FP algorithm iteratively stitches together the images from different areas of the Fourier space in order to achieve a large effective NA_{synth} equal to the sum of the objective NA_{meas} and illumination NA_{illum} . The phase in FP is inferred by a phase retrieval optimization [10] based on angular diversity, analogous to Ptychography based on spatial translation [11].

The FP recovery procedure, shown in Fig. 2, starts by initializing a complex HR image $\sqrt{I_h} e^{j\phi_h}$ by up-sampling (interpolating) one of the LR images and adding a constant phase.

Simulating the Iterative FP Algorithm

A complex HR scene to be reconstructed by the FP algorithm, shown at Fig. 3-left, is consisted of a cameraman image as intensity profile scaled between (0,1) and an aerial image as phase information ϕ scaled between $(-\pi, \pi)$. The LR images captured at 81 unique illumination angles are acquired by extracting various circular regions in the Fourier space, samples are presented in Fig. 3- right.

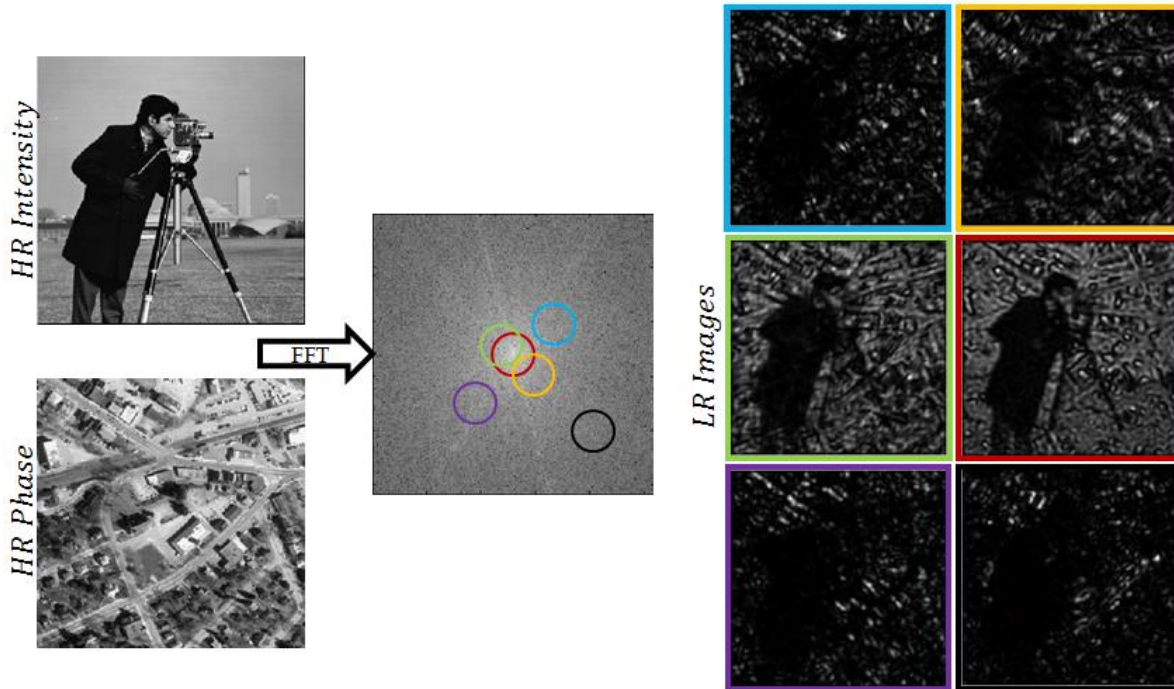


Fig. 3. A complex HR scene (left), its Fourier transform (center), and samples of LR images (right). The LR images are framed in different colors to indicate their correspondent locations in the Fourier space.

The LR images, indexed by i , are fused in the iterative FP algorithm (one at each iteration) to update the corresponding frequency regions and improve the reconstructed HR intensity and phase at $2 \times$ SR factor, samples are shown in Fig. 4. The relative numerical error is calculated by $RMSE = \sqrt{\frac{1}{PQ} \sum_{x=1}^P \sum_{y=1}^Q (\text{ReconImage}(x, y) - \text{HRImage}(x, y))^2} / DR$ where $DR = 1$ for intensity and 2π for full scale phase at each iteration. See Fig. 5 to evaluate the reconstruction errors as a function of iteration index = $(c - 1) * 81 + i$ where i indexes the inner loop and c indexes the outer one.

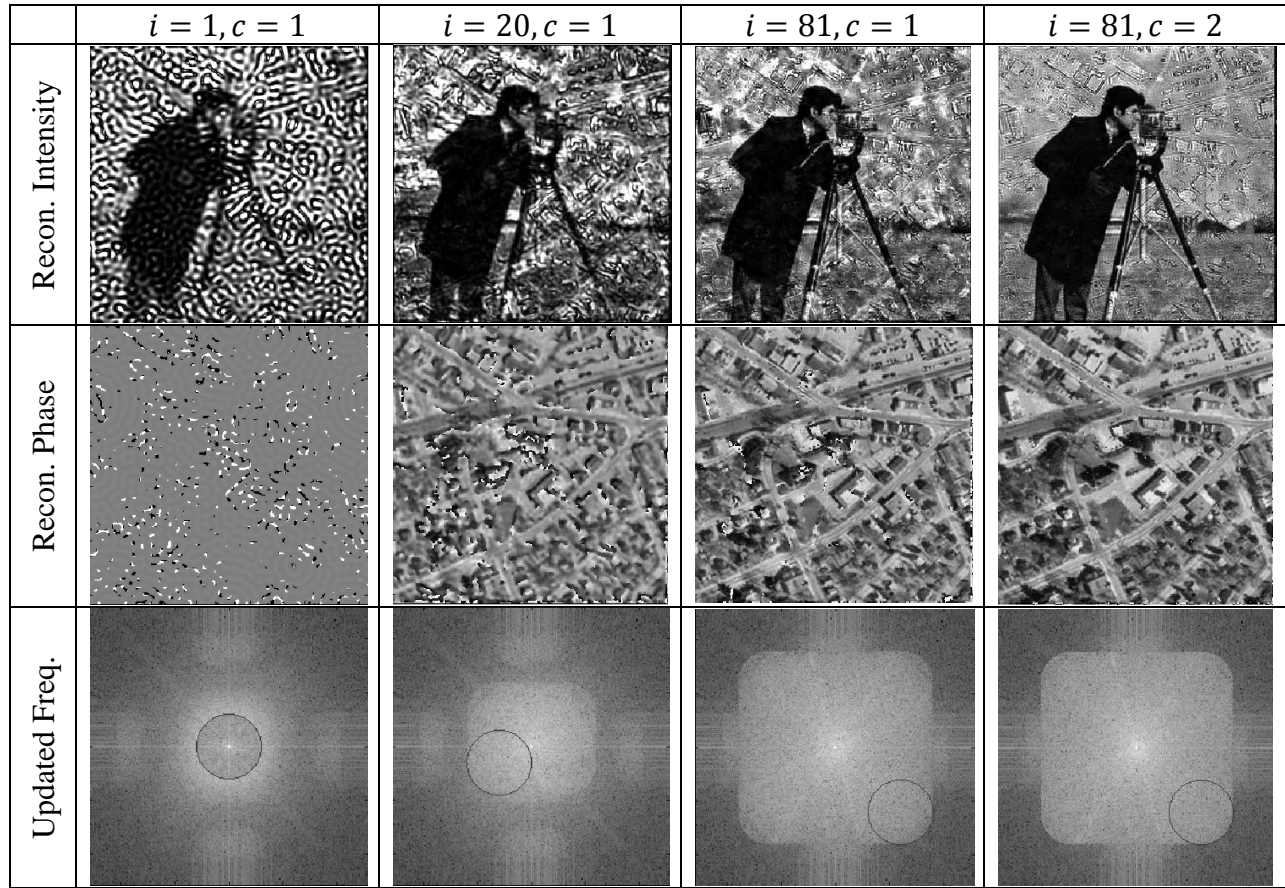


Fig. 4. Iterative reconstruction results for intensity (first row), phase (second row), and the frequency space showing the circle profile being updated (third row). The original phase was scaled between $(-\pi, \pi)$.

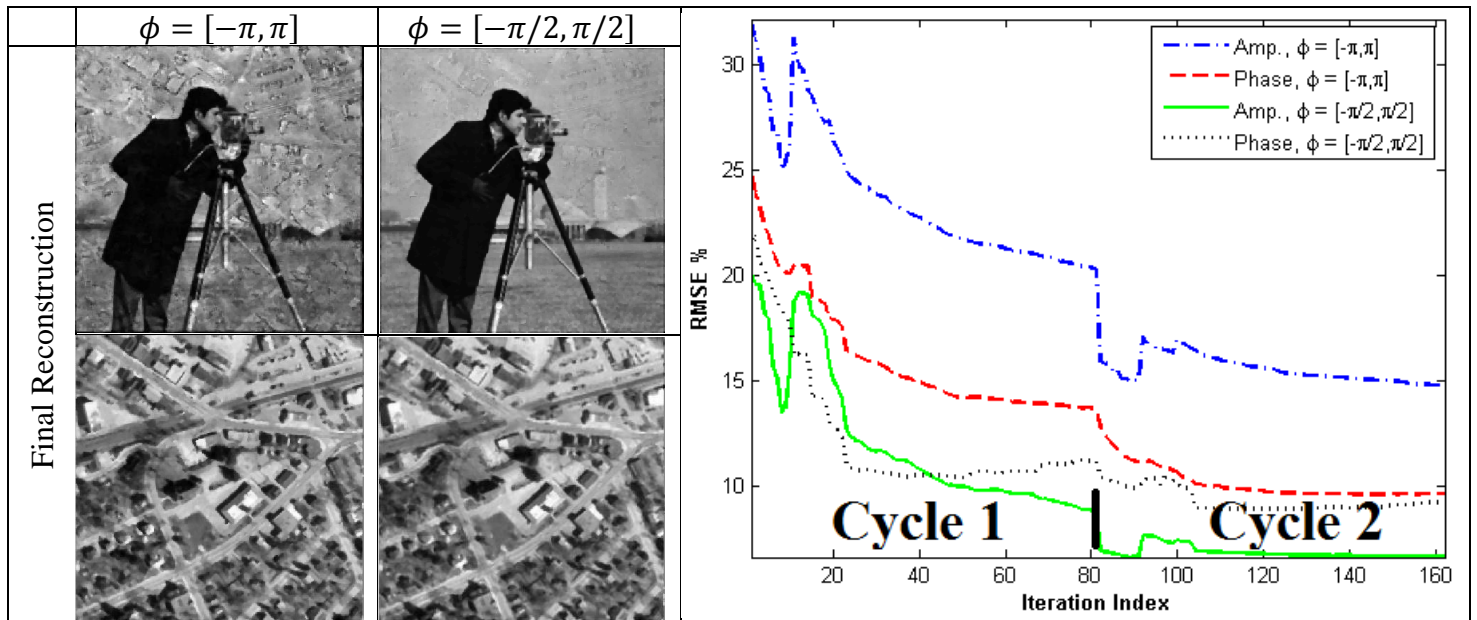


Fig. 5. Final FP reconstructions of cameraman intensity and aerial phase images after median filtering with original phase scaled to $(-\pi, \pi)$ (left), to $(-\pi/2, \pi/2)$ (center), and reconstruction errors as function of iteration index (right).

The iterative RMSE curves, in Fig. 5, show that on average the RMSE decreases with more iterations till nearly flattened (i.e. no significant improvement) at the end of the 2nd cycle. Note that the final resulted errors are due to not scanning the full HR frequency domain (i.e. no measurements at very steep angles were captured) besides the reconstruction artifacts (the phase artifacts in the reconstructed intensity and intensity artifacts in the reconstructed phase) which may be attenuated by the median filtering step. To further suppress these artifacts, the original phase was rescaled to $(-\pi/2, \pi/2)$ and the whole iterations were repeated giving significant improvement in the intensity image (see the background in cameraman image in Fig. 5).

Case Studies on Selected FP Parameters

To gain a better understanding about the FP algorithm and figure the best approaches to implement it for reflective-mode imaging setup, the impact of various FP parameters is analyzed. The evaluated parameters are: SR Factor, update path, path radius in case of circular update path, and the number of LR images. U.S. Air force 1951 (USAF) target was used as intensity image along with a constant phase to form the complex HR image. Unless specified differently in each case, the reconstruction parameters used in the case studies were set as follows: SR Factor = 2 \times , number of LR images = 81, outward spiral update path, circular radius of the objective lens (in Fourier space) = 30 pixel, and measurement spacing (in Fourier space) = circular radius / 2.

Impact of Superresolution Factor

Given the same number of measurements, illumination angles, update path, and objective lens, the SR (sampling) factor was set to be 2 \times , 3 \times , and 4 \times . This was done by truncating or zero padding the edges in the Fourier space to down-sample or up-sample respectively at each iteration. Fig. 6,7 demonstrate that higher SR factors require more measurements and iterations

to converge and deliver better HR reconstructions. Note SR Factor only controls the # pixels while resolving the fine features is determined by how steep the illuminating rays are.

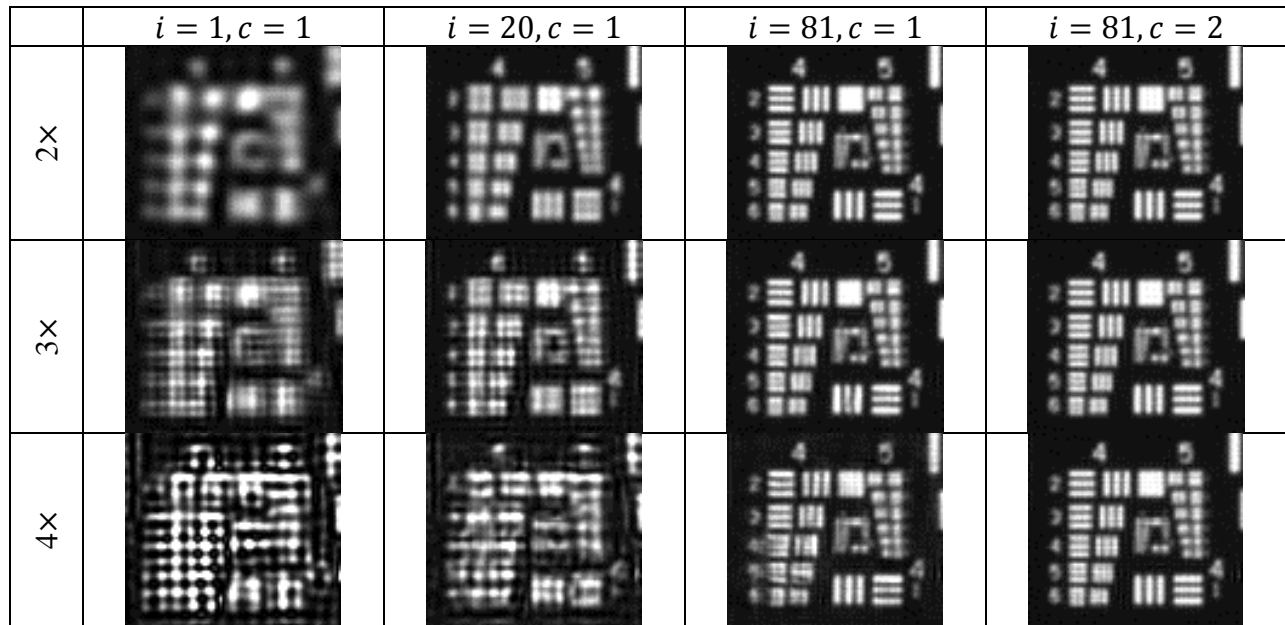


Fig. 6. Iterative reconstruction results for USAF (zoomed) at different SR factors.

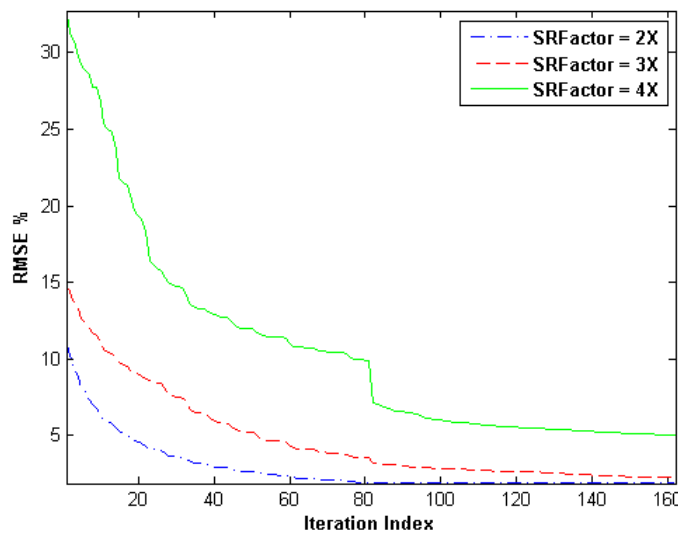


Fig. 7. Iterative reconstruction errors as a function of iteration index for various SR factors.

Impact of the Update Path

Four different update paths; outward spiral, inward spiral, rectangular path, and circular path, shown in Fig. 9– left, were implemented to investigate the impact of updating certain frequency regions before others through the iterative process. Fig. 8,9 demonstrate that nearly all paths

converge to 2-4% RMSE range after enough iterations and cycles. However, the outward spiral path which updates starting from the lowest frequency regions (bright field measurements) was the first to converge at best performance (i.e. resolving group 4 – elements 4 of the USAF).

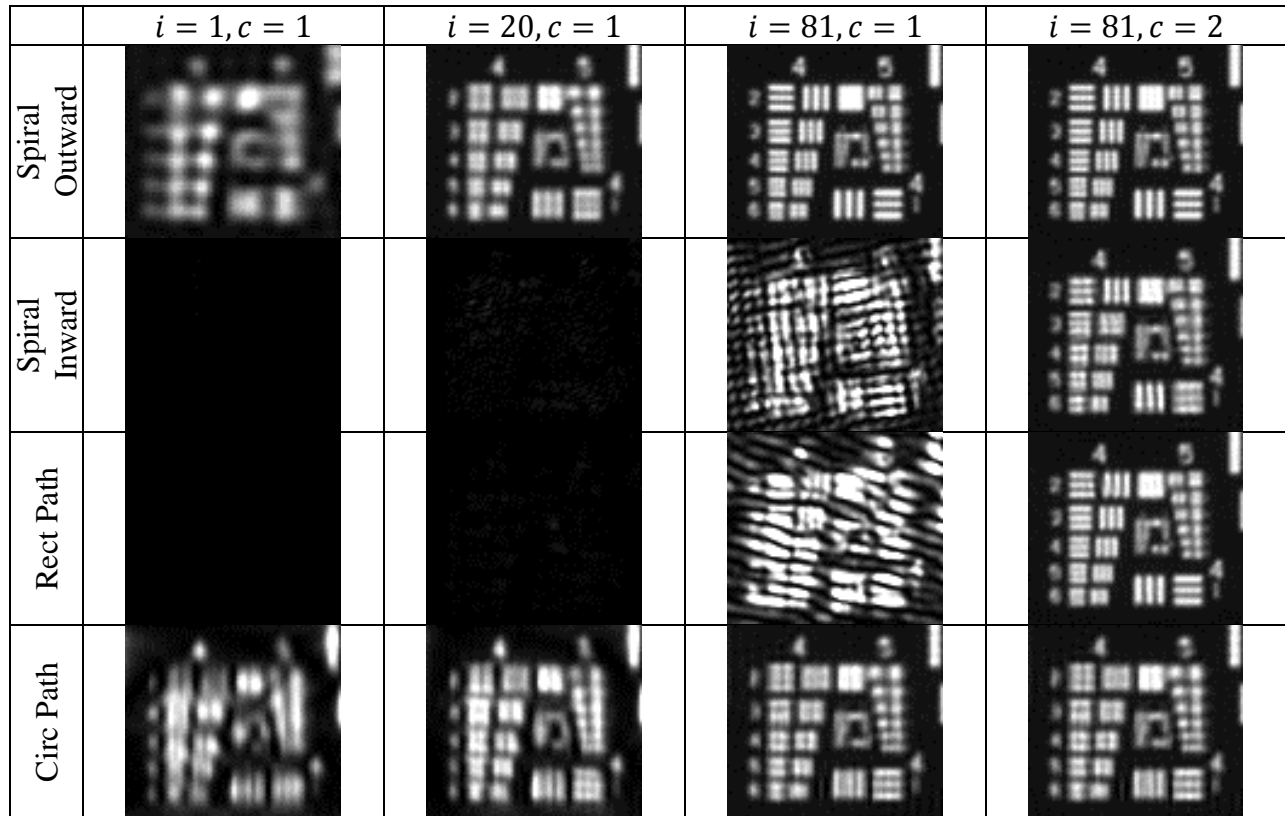


Fig. 8. Iterative reconstruction results for USAF (zoomed) at different update paths.

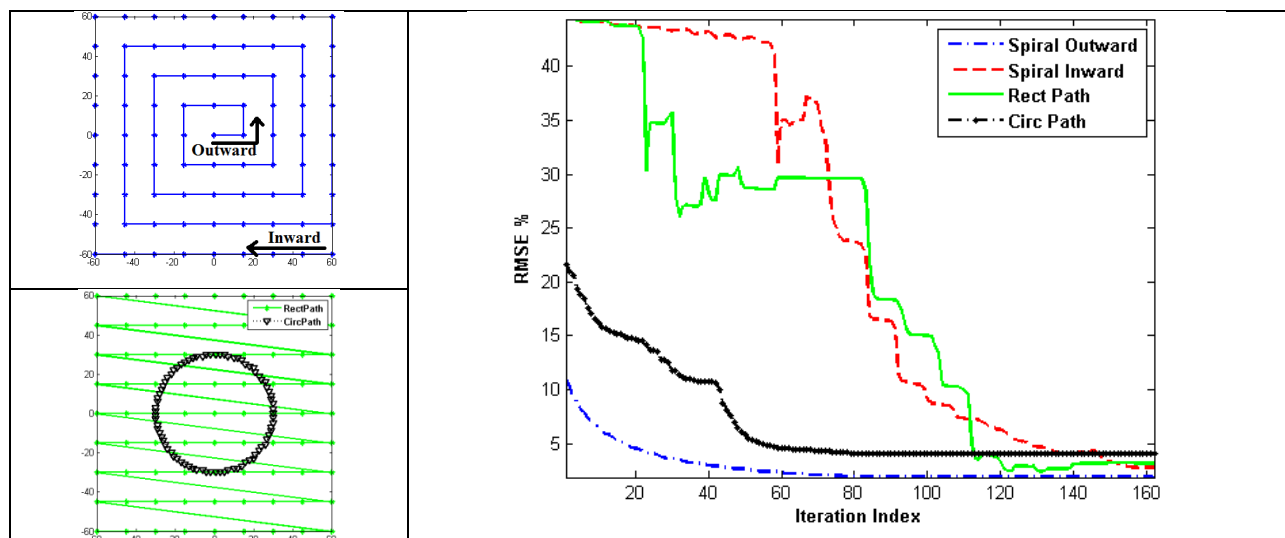


Fig. 9. Update paths (left) and the associated iterative reconstruction errors as a function of iteration index (right).

Impact of Circular Path Radius

For inspection devices incorporating front-end camera, it will be hard to acquire bright field measurements centered at DC and low frequency regions since the camera body will block these illumination angles (in the reflective mode). Such systems may be practically limited to circular illumination paths which are being studied here for various path radii in the Fourier space, shown in Fig. 11-left. Fig. 10,11 show that using a small radius, e.g. 15 pixels, results in a lot of overlapped measurements in the low frequency regions leading to fast convergence but without any mid-high frequency content. On the other hand at high radii, e.g. 60 pixels, no bright field measurements can be captured, hence the high frequencies only are updated, leading to the worst RMSE performance regardless of how many iterations are involved. A mid radius, e.g. 30 pixels, initially iterates with relatively high RMSE as fewer low frequencies are updated simultaneously. However with more iterations, it can eventually outperform all as it covers the mid frequency range too.

The bottom line, having both bright and dark field measurements is important to get the best SR reconstructions.

	$i = 1, c = 1$	$i = 20, c = 1$	$i = 81, c = 1$	$i = 81, c = 2$
CircPathR = 15 Pixels				
CircPathR = 30 Pixels				

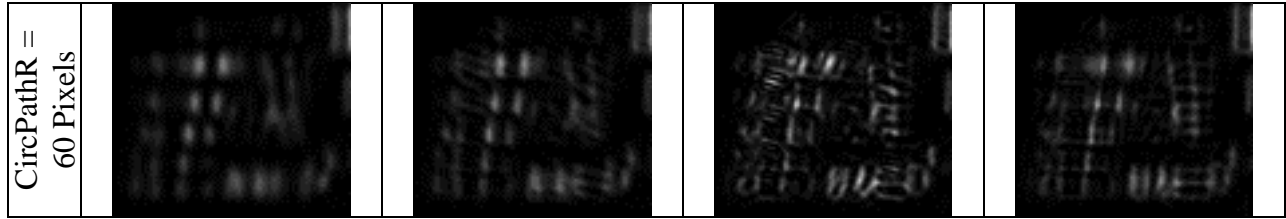


Fig. 10. Iterative reconstruction results for USAF (zoomed) at different path radii.

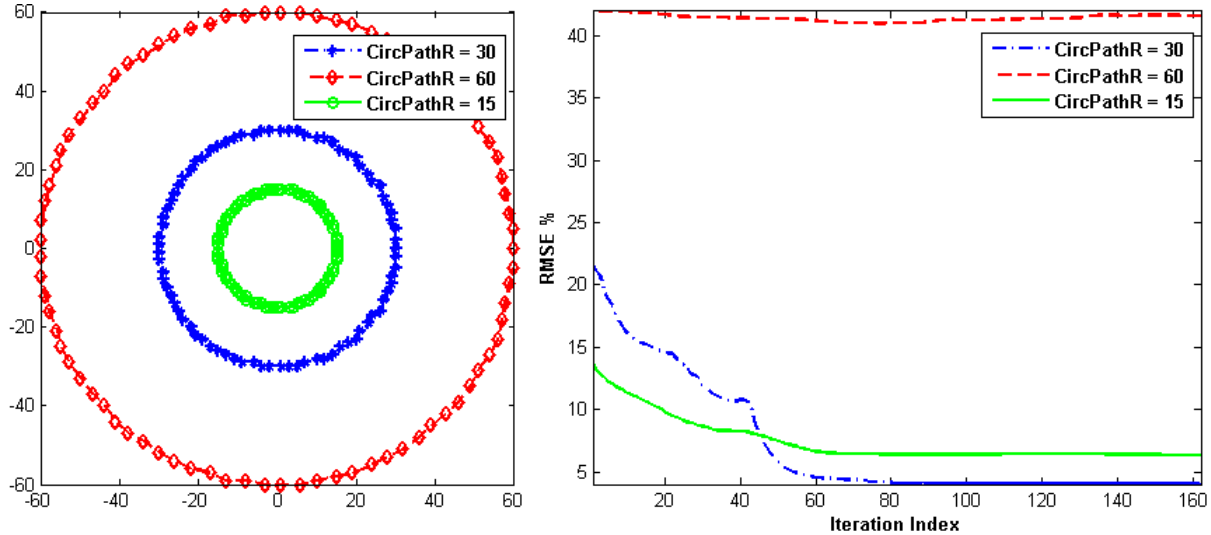


Fig. 11. Circular paths of different radii in pixels (left) and the associated iterative reconstruction errors as a function of iteration index (right).

Impact of Number of LR Images

Reducing the number of (#) measurements without sacrificing the reconstruction quality is critical for real-time imaging applications. However, FP requires significant overlap (> 60%) [4, 12] between the Fourier space areas of neighboring illumination angles to converge. To visualize its impact, the number of LR images was set to be 9, 27, and 81 covering two different update paths (outward spiral and circular) as shown in Fig. 13-left. The iterative RMSE curves, plotted as a function of normalized iteration index in Fig. 13-right, and the visual reconstructions, displayed in Fig. 12, show a degraded performance (more significant in the outward spiral path) as the number of measurements is largely decreased (e.g. to 9 images). Yet, there is insignificant degradation when using 27 image as compared with the 81 case. Therefore, the number of measurements (taken in sequential mode) may be optimized with tolerable RMSE performance.

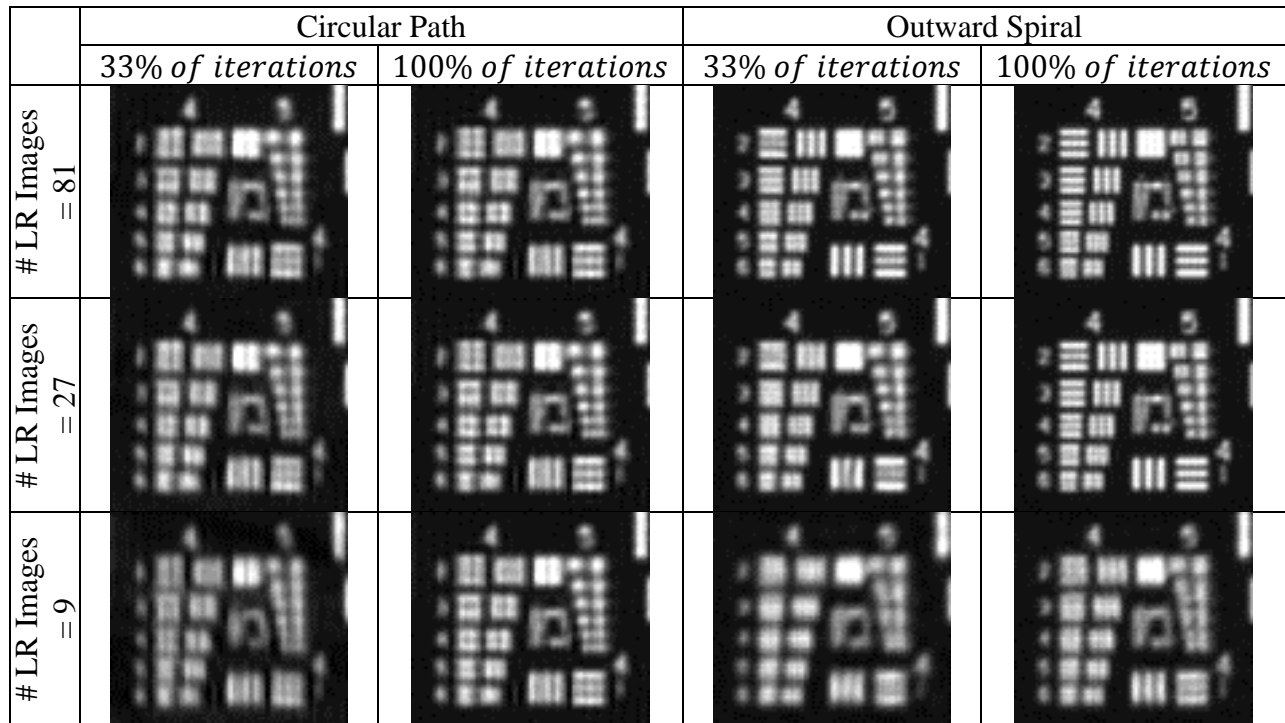


Fig. 12. Reconstruction results for USAF (zoomed) after 33% and 100% of iterations at different # measurements (across the rows) for two different update paths; the circular path (first two columns) and outward spiral path (last two columns).

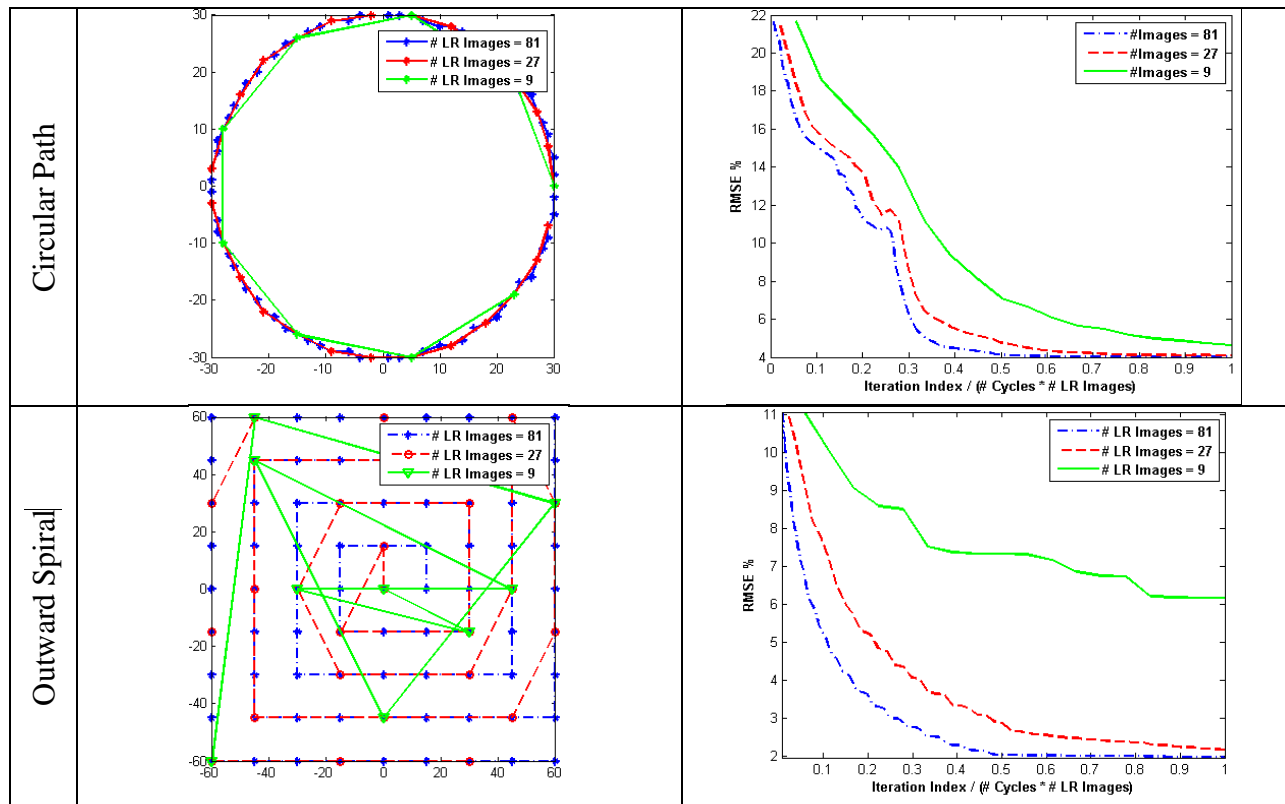


Fig. 13. Update paths (left column) and iterative reconstruction errors as a function of normalized iteration index (right column) for different number of images taken in a circular path (top row) and in an outward spiral path (bottom row).

Experimental Results

The experimental setup is shown in Fig. 14. All samples were imaged with a $0.1 NA_{meas}$ microscopic objective of focal length $f = 45 \text{ mm}$ and a scientific CMOS camera (PCO edge) at 16 bit level with $6.5 \mu\text{m}$ pixel pitch. The system magnification was $3.294\times$ and the entrance pupil diameter was 6.5 mm . Two programmable motions were introduced to shift the illuminating sources: A XY translation imposed by two orthogonal actuators to generate directional illuminations within the objective lens and a circular motion generated by a rotation stage to produce large illumination angles beyond the objective lens's diameter. A green LED of 535 nm wavelength was used in both motions. Also, a transparent negative $3'' \times 3''$ USAF target was used as a thin planar object with $\sim 100\%$ reflectivity at the bars.

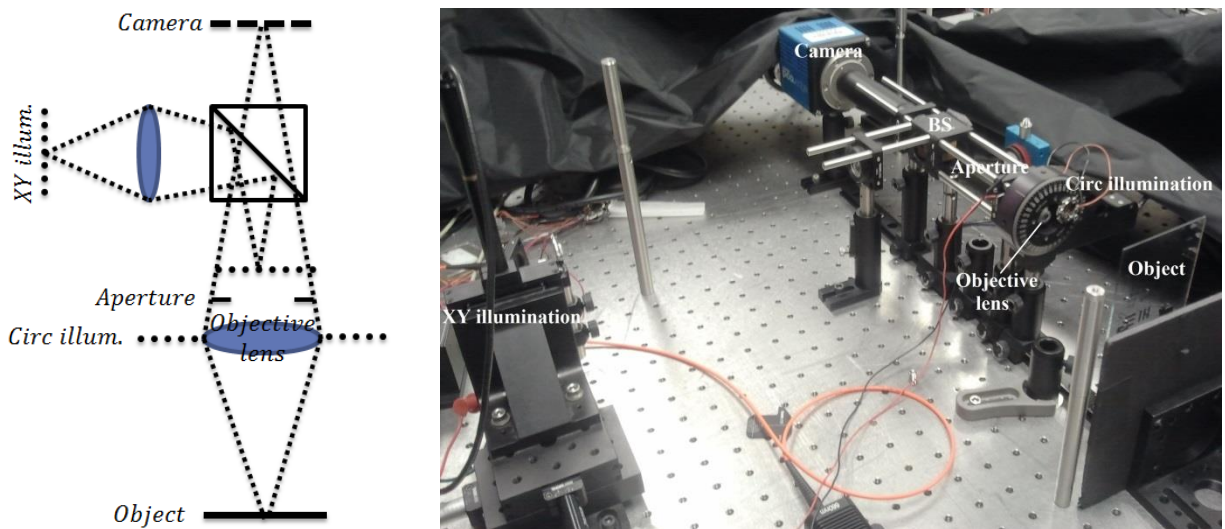


Fig. 14. Sketch (left) and the experimental relective-mode imaging setup (right) showing the XY and Circ illuminations.

The experimental data and physical imaging parameters were fed into Tian's FP algorithm [13] which solves a minimization problem over all measurements. This was done in patch-wise approach where reconstructed FOV was splitted into patches whose area is on the order of the spatial coherence area of a single directional illumination. Afterward, the reconstructed patches were stitched together to form the super-resolved image at a given SR factor (here was set to $6\times$).

XY Measurements

The green LED mounted on the XY translation stages was located at a distance so its real image through the relay lens and the beam splitter (BS) resides at the focal length of the microscopic objective, hence, its Fourier transform becomes a plane wave illuminating the target. The spacing between the successive LED transitions at the LED image plane was $725\ \mu\text{m}$. In total, 9×9 LR Images were captured, most of them represent bright field measurements and shown in Fig. 15, where each was uniquely illuminated from one of the XY transitions of the LED.

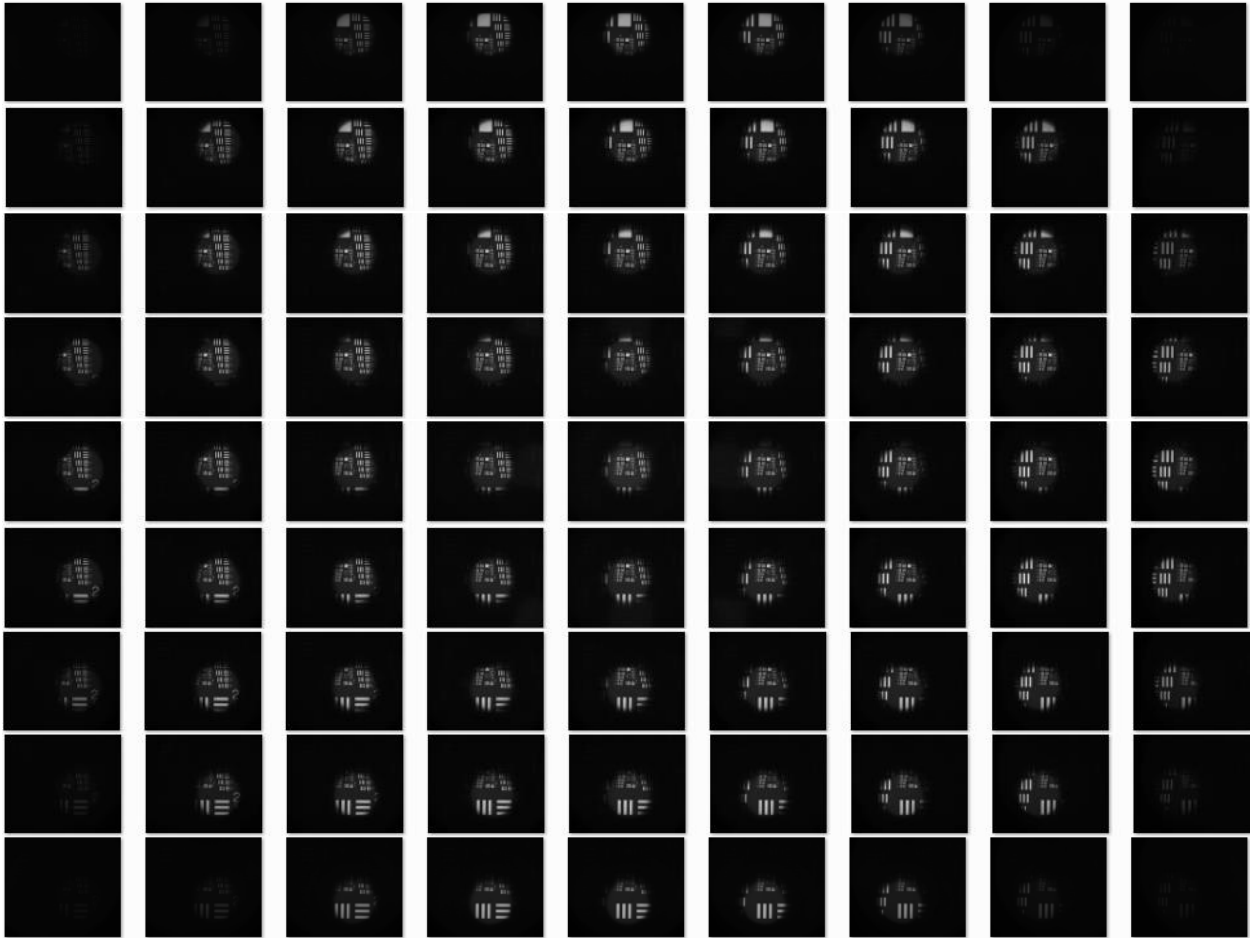


Fig. 15. 9×9 LR Images captured by XY translations of a green LED.

Following an outward spiral scanning update, the FP algorithm was capable of synthesizing a $NA_{synth} = 0.235$ resolving all elements in group 7 of the USAF target as compared with the LR

measurements captured via $NA_{meas} = 0.1$ which was resolving up to elements 2 only of group 7. See Fig. 16 for visual comparison.

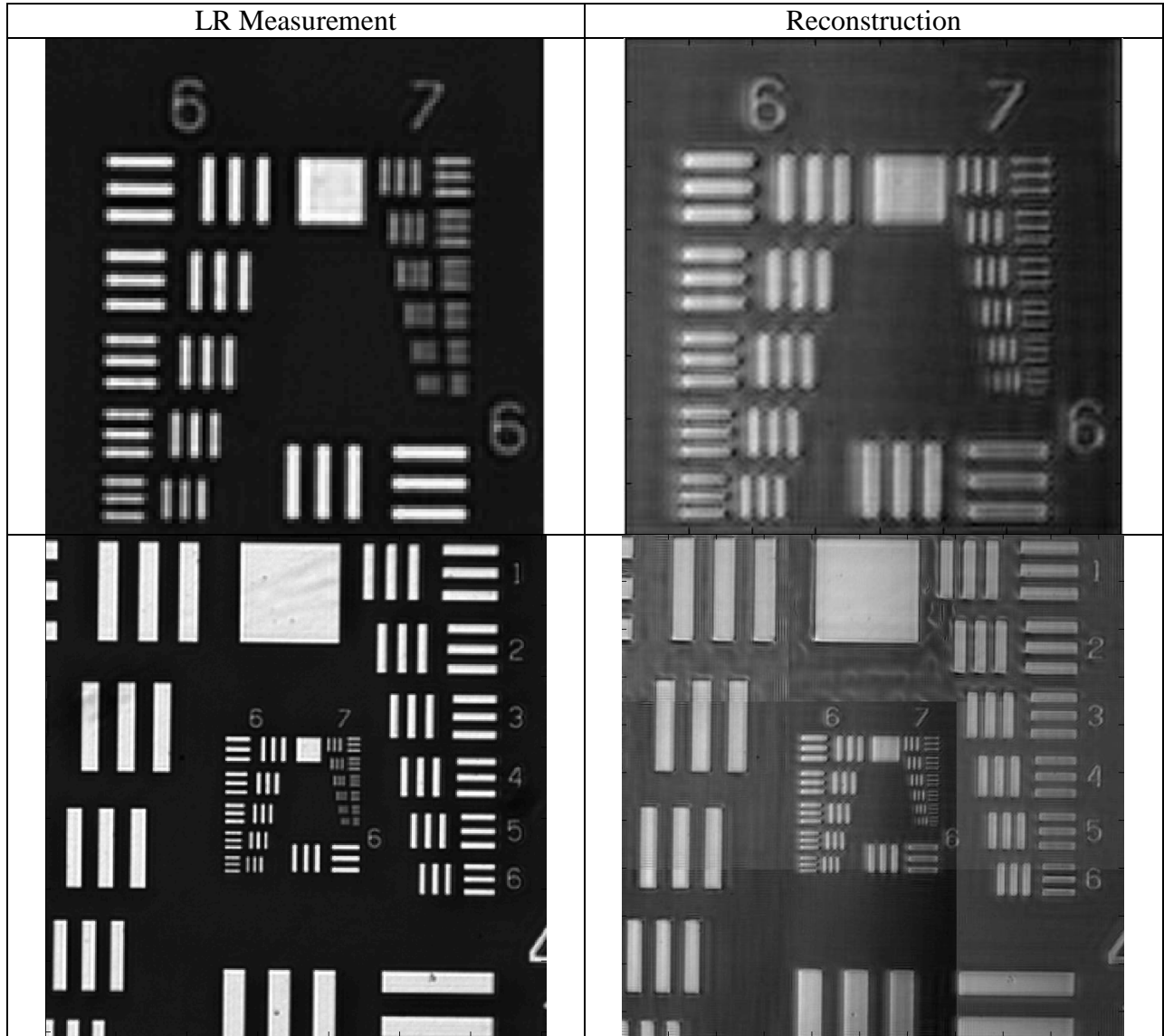


Fig. 16. FP using XY measurements; LR centered patch (top-left), and its FP reconstruction (top-right), 3x3 LR patches (bottom-left), and their FP reconstructed image after stitching (bottom-right).

Now to evaluate the impact of LR images picked from different parts of the spiral path, the captured images were distributed into groups where each group had different number of images N_{img} with circular path of radius R . i.e. $R = 0$ means the DC measurement, $R = 1$ means the LR images of indices ± 1 in the spiral path, and so on. The reconstruction results of each group

separately, shown in Fig. 17, agrees with FP principles that is as the circular radius increases (illumination angle increases), higher spatial frequencies can be resolved but the SNR becomes weaker. In principle, larger translation to the LED could provide larger NA improvement, but it was practically limited here by the vignetting of the microscopic objective's body and the noise in the dark field images at high illumination angles, see cases of $R=6,7$ in Fig. 17.

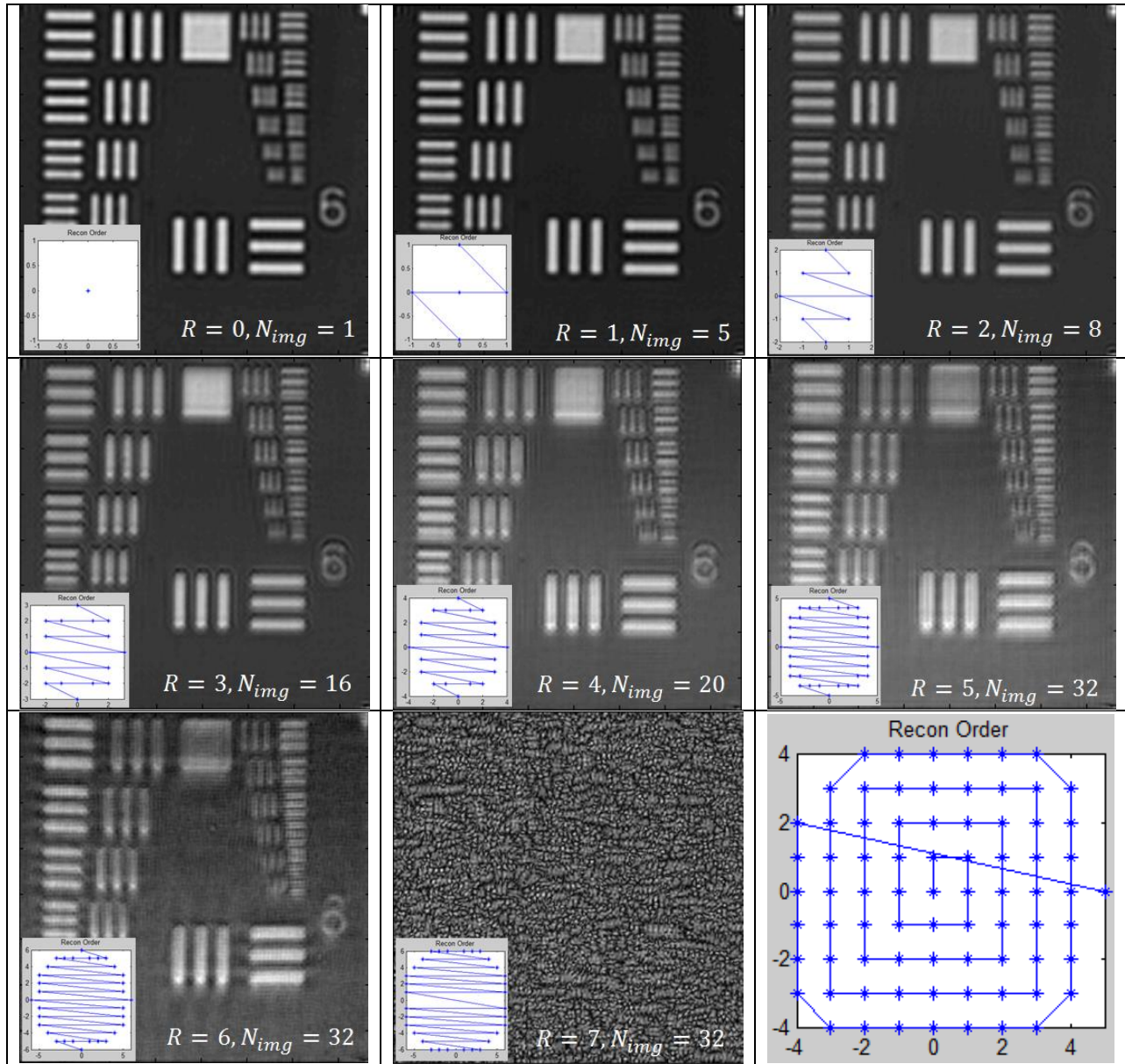


Fig. 17. FP reconstructions at selected images and circular paths. The selected locations are shown at the bottom-left of each image. The whole spiral update path is shown at the bottom-right image.

Circular Measurements

Here, the green LED was mounted on a rotation stage with a circular radius 11 mm (from the center of the objective lens) with 6 mm distance to the USAF target resulting in a very steep illumination angle with $NA_{synth} = 0.77$. Also, the small LED-target distance (due to physical constraints) makes the illuminating waves kind of spherical rather than plane waves which invalidates the illumination assumptions made in FP algorithm. The separating rotation angle between successive LR measurements was 5° resulting in 72 LR images in total, see Fig. 18.

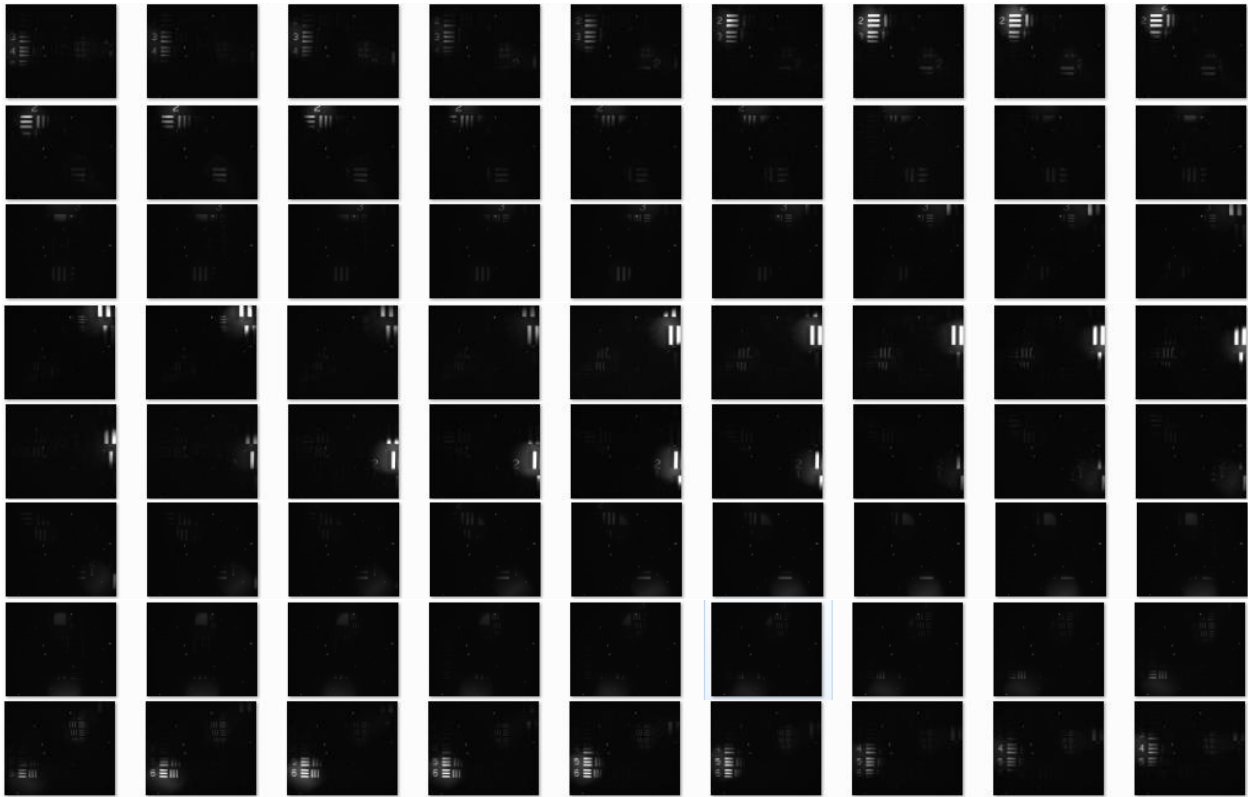


Fig. 18. 72 LR images captured by a circular translation of a green LED.

Following a circular update path and inputting the dark field measurements, the FP algorithm was capable of reconstructing the edges of the bars, see Fig. 19, with limited success in resolving the elements of group 7 in the USAF target due to the weak SNR and the improper assumption of having plane wave illumination during the reconstruction.

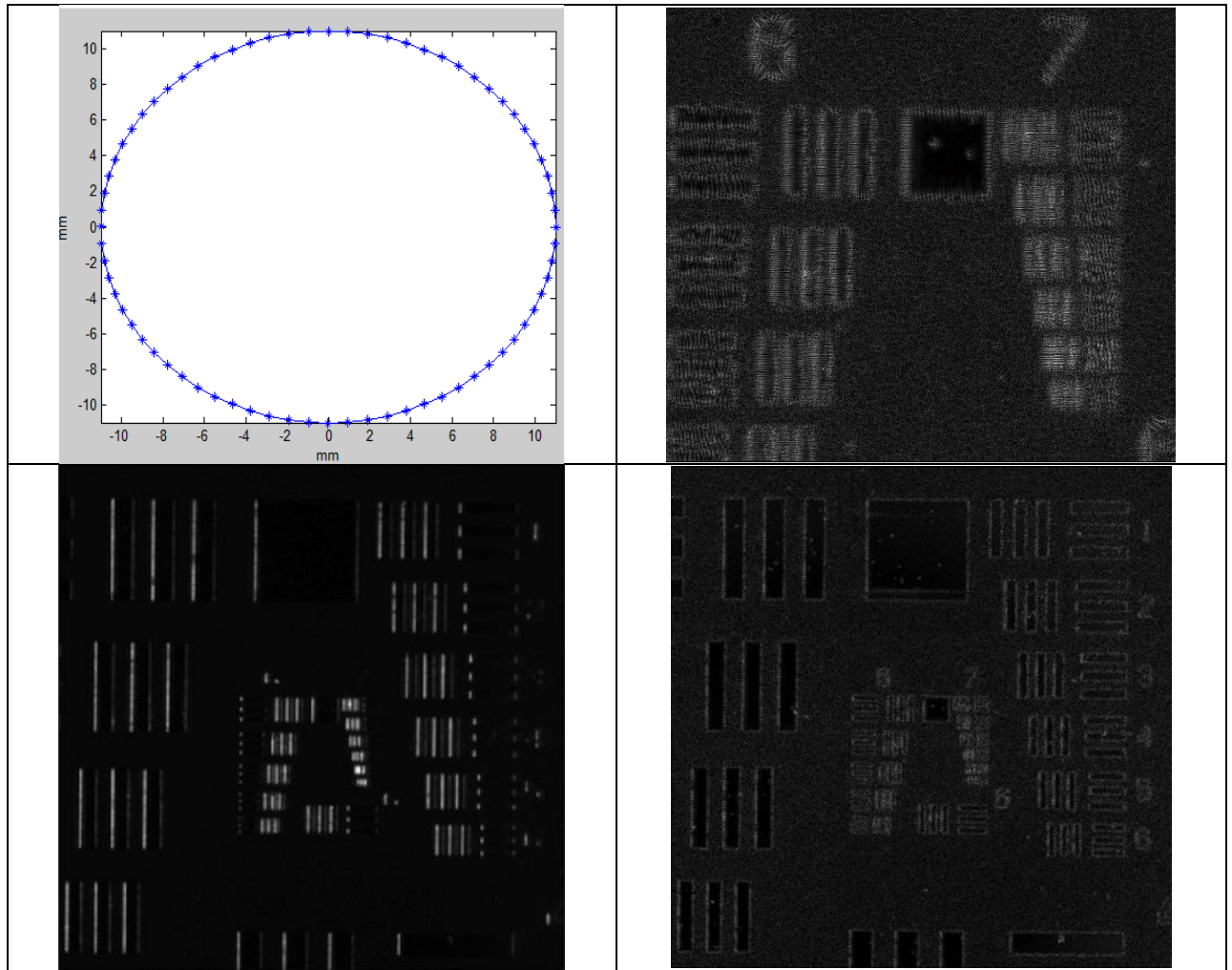


Fig. 19. FP using circular measurements; circular path (top-left), FP reconstruction for the centered patch (top-right), LR Image (bottom-left), and its 3×3 patch FP reconstructed image (bottom-right).

Fourier Ptychography for Diffusing Objects

The scenes under inspection have usually partially diffusing surfaces where each incident ray may be reflected into different directions and in various intensities forming a diffusing profile, sample is shown in Fig. 20-left. This may be approximated by assuming a non-diffusing thin surface of 100% reflectivity being virtually illuminated simultaneously from multiple adjacent directions with different intensities. Thus, each captured image multiplexing these diffused rays should be used to update multiple overlapping frequency regions simultaneously at the Fourier space, see Fig. 20-right.

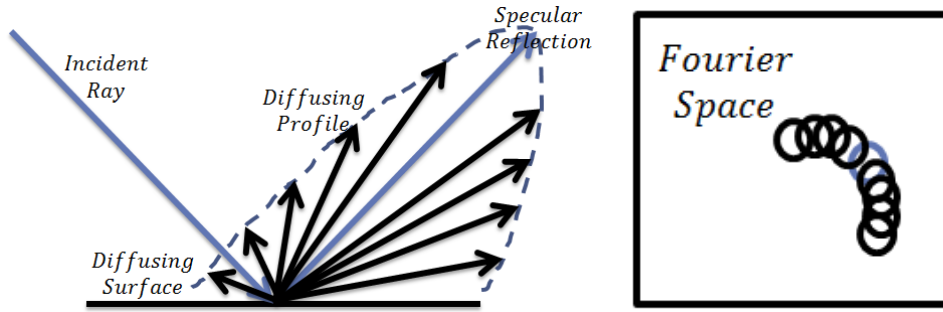


Fig. 20. A reflection sample of diffusing surface (left) and the correspondent frequency regions in Fourier space (right).

The multiplexed diffused measurements may be imposed in FP algorithm, following the notation used in [13], as follows: A thin reflective surface $O(\mathbf{r})$ where $\mathbf{r} = (x, y)$ is sequentially illuminated by plane waves of unique spatial frequencies $\mathbf{k}_m = \left(\frac{\sin \theta_{xm}}{\lambda}, \frac{\sin \theta_{ym}}{\lambda} \right)$ where θ_{xm}, θ_{ym} are the illumination angles, λ is the wavelength, and $m = 1, \dots, N_{img}$ (number of illumination angles). The diffused reflected waves, with indices ℓ_m forming the diffused angles with diffusing profile w , are then low pass filtered by the objective lens of pupil function $P(\mathbf{k})$. Finally, the multiplexed image at the m^{th} illumination will be the sum of weighted diffused intensities given by: $I_m(\mathbf{r}) = \sum_{i \in \ell_m} |\mathcal{F}(w(i)O(\mathbf{k} - \mathbf{k}_i)P(\mathbf{k}))|^2$.

The FP algorithm in this case has to find $O(\mathbf{r})$ that minimizes the mean square solution between the actual and the estimated measurements over all the diffused angles, the spatial info, and the LR measurements as follows:

$$\min_{O(\mathbf{k})} \sum_{m=1}^{N_{img}} \sum_{\mathbf{r}} \left| I_m(\mathbf{r}) - \sum_{i \in \ell_m} |\mathcal{F}(w(i)O(\mathbf{k} - \mathbf{k}_i)P(\mathbf{k}))|^2 \right|^2$$

Other approaches to address the scattering and diffusing problems can be found in [14, 15].

The experimental setup, prescribed in the previous section, was used with a transparent USAF target sprayed by CEREC Optispray material to emulate diffusion, see Fig. 21-left. The material also acted as attenuator causing significant information loss in the captured LR images, sample is shown in Fig. 21-center. The HR image resolving elements in group 6, presented in Fig. 21-right, was reconstructed by a sequential FP algorithm integrating 81 LR image in outward spiral scanning path by considering the specular reflection only (diffusing profile was not characterized here since the sprayed material was blocking many of the reflected directional information). A better diffusing target with microscopic structure (since the FP algorithm worked the best experimentally with microscopic objectives) shall be characterized and used in the future.



Fig. 21. USAF target with Optispray diffusing material on it to emulate diffusion (left), sample of LR image taken with $NA_{meas} = 0.037$ (center), and the resulted FP reconstruction of $NA_{synth} = 0.1$ (right).

Conclusion and Future Research Directions

Fourier Ptychography (FP) forms a powerful computational imaging tool to bring superresolution capability to the surface metrology and inspection devices. It does this by integrating a number of variably illuminated low-resolution (LR) intensity images in the Fourier space to produce, through an iterative phase retrieval algorithm, a wide-field high-resolution (HR) complex image.

The simulation and experimental results show; 1- the need for more dark field measurements taken at steeper illumination angles to resolve finer features besides the bright field images which update the low frequency regions containing most of the energy, 2- the fast convergence when updating the HR Fourier space following an outward spiral path, 3- the possibility of reducing the number of measurements (if well distributed with sufficient overlap in the Fourier space) without sacrificing much of the reconstructed quality, and 4- the ability to synthesize a larger numerical aperture (NA) (e.g. 0.235) from LR images captured with objective lens of smaller NA (e.g. 0.1).

As for future research, the diffusing profiles of various surfaces need to be experimentally characterized and fed into the FP algorithm, derived in this report, to uniquely weight the various reflections which correspond to overlapping areas in the Fourier space. The uniform diffusing (flat) profile such that in Lambertian surfaces may cause the FP algorithm to fail as all frequency regions get updated regardless of the directional illuminations.

Also, the inspected surfaces may cause illuminating rays to penetrate through various structures before being partially scattered, reflected, or attenuated. Such behavior may be approximated through a multi-slice model [7] where rays are traced through each thin slice to track the directional and intensity information critical for the FP reconstructions.

Furthermore, collecting LR images illuminated by steep angles may be challenging due to the physical constraints in reflective-mode fiberscopes. This might be introducing different upper limits of how much improvement can be delivered by the FP technique in different inspection devices to be investigated in the future.

Finally, the real-time aspect may be critical for some inspection applications. Therefore the sequential acquisition scheme (illuminating from a single location at a time) implemented here should be replaced by a multiplexing approach [13] where multiple light sources selected at random locations illuminate the object at the same time. This may add to the reconstruction complexity but comes with many benefits such as acquiring less data at higher signal to noise ratio and shorter acquisition times.

Acknowledgement

The author would like to kindly thank Dr. Ron Liang for his support of this research, Shaun Pacheco for his assistance in collecting the experimental data, Lei Tian and Guoan Zheng for the helpful discussions and the Matlab codes used to reconstruct the experimental data.

References:

- [1] A. W. Lohmann, R. G. Dorsch, D. Mendlovic, Z. Zalevsky, and C. Ferreira, "Space-bandwidth product of optical signals and systems," *J. Opt. Soc. Am. A*, vol. 13, no. 3, p. 470–473, 1996.
- [2] G. Zheng, *Innovations in Imaging System Design: Gigapixel, Chip-Scale and Multi-Functional Microscopy*, Dissertation at California Institute of Technology, 2013.
- [3] Z. Zalevsky and D. Mendlovic, *Optical Superresolution*, Springer Series in Optical Sciences, Vol. 91, 2003.
- [4] G. Zheng, R. Horstmeyer, and C. Yang, "Wide-field, high-resolution Fourier ptychographic microscopy," *Nature Photonics*, vol. 7, p. 739–745, 2013.
- [5] T. Turpin, L. Gesell, J. Lapides, and C. Price, "Theory of the Synthetic Aperture Microscope," *Proc. SPIE*, vol. 2566, p. 230–240, 1995.
- [6] X. Ou, R. Horstmeyer, C. Yang, and G. Zheng, "Quantitative phase imaging via fourier ptychographic microscopy," *Opt. Lett.*, vol. 38, pp. 4845–4848, 2013.
- [7] L. Tian and L. Waller, "3D intensity and phase imaging from light field measurements in an LED array microscope," *Optica*, vol. 2, pp. 104–111, 2015.
- [8] Z. Phillips, M. D'Ambrosio, L. Tian, J. Rulison, H. Patel, N. Sadras, A. Gande, N. Switz, D. Fletcher, L. Waller, "Multi-contrast imaging and digital refocusing on a mobile microscope with a domed LED array," *PLOS one*, 2015.
- [9] X. Ou, G. Zheng, and C. Yang, "Embedded pupil function recovery for Fourier ptychographic microscopy," *Optics Express*, vol. 22, p. 4960–4972, 2014.
- [10] J. R. Fienup, "Phase retrieval algorithms: a comparison," *Appl. Opt.*, vol. 21, p. 2758–2769, 1982.
- [11] M. Guizar-Sicairos and J. R. Fienup, "Phase retrieval with transverse translation diversity: a nonlinear optimization approach," *Opt. Express*, vol. 16, p. 7264–7278, 2008.
- [12] O. Bunk, M. Dierolf, S. Kynde, I. Johnson, O. Marti, and F. Pfeiffer, "Influence of the overlap parameter on the convergence of the ptychographical iterative engine," *Ultramicroscopy*, vol. 108, p. 481–487, 2008.
- [13] L. Tian, X. Li, K. Ramchandran, and L. Waller, "Multiplexed coded illumination for Fourier Ptychography with an LED array microscope," *Biomedical Optics Express*, vol. 5, no. 7, pp. 2376–2389, 2014.
- [14] P. Li, D. J. Bateya, T. B. Edob, and J. M. Rodenburg, "Separation of three-dimensional scattering effects in tilt-series Fourier ptychography," *Ultramicroscopy, Elsevier*, vol. 158, pp. 1–7, 2015.
- [15] H. Liu, E. Jonas, L. Tian, Z. Jingshan, B. Recht, and L. Waller, "3D imaging in volumetric scattering media using phase-space measurements," *Optics Express*, vol. 23, no. 11, pp. 14461–14471, 2015.